Supplementary Information (SI) for EES Catalysis.
This journal is © The Royal Society of Chemistry 2025

Supplementary Materials for

Tailoring Electronic Structure of Exfoliated Layered Double Hydroxide by Lanthanide for Chloride-Ion Blocking in Seawater Splitting

Ashish Gaur, ≠,[a] Jiseok Kwon,≠,[b] Jatin Sharma,[a] Ghulam Ali,[c] Enkhtuvshin Enkhbayar,[a] Chan-Yeup Chung[d], HyukSu Han*,[a], Taeseup Song*,[b]*

a. *Department of Energy Science, Sungkyunkwan University, 2066 Seobu-ro, Jangan-gu, Suwon-si, Gyeonggi-do 16419, Republic of Korea*
b. *Department of Energy Engineering, Hanyang University, 222 Wangsimni-ro, Seongdong-gu, Seoul 04763, Republic of Korea*
c. *U.S.-Pakistan Center for Advanced Studies in Energy (USPCASE), National University of Sciences and Technology (NUST), H-12, Islamabad, Pakistan*
d. *Bass Co. LTD., 1121 Beoman-ro, Geumcheon-gu, Seoul, 08594, Republic of Korea*

≠ = both the authors contributed equally

**Corresponding author. chanyeup.chung@gmail.com (C.Y.C), hyuksuhan@skku.edu (H.H.), tssong@hanyang.ac.kr (T.S)*

Contents

Materials and Methods

Chemicals

Nickel (II) nitrate hexahydrate ($Ni(NO_3)_2.6H_2O$, 98%), Iron (III) chloride hexahydrate ($FeCl_3.6H_2O$, 99%), Cerium (III) nitrate hexahydrate ($Ce(NO_3)_3.6H_2O$, 99%), Hexamethylenetetramine ($C_6H_{12}N_4$, 99%) dium hydroxide(NaOH, 99.9%), Sodium chloride (NaCl, 99%), Hydrochloric acid (HCl, 37%) were purchased from Sigma-Aldrich (Germany). Nickel foam was purchased from Alfa Aesar. All chemicals were used as purchased without further treatment.

Fabrication of the NF-LDH:

The as obtained nickel foam was first subjected to acid treatment for removing the oxide layer and impurities form the surface. The NF has been sonicated for the 5 min with the HCL solution (37 wt%). Hydrothermal method was used for the fabrication of the NF-LDH. In 50 ml deionized water (DI) 4 mmol of $Ni(NO_3)_2.6H_2O$, 1 mmol of $FeCl_3.6H_2O$ and 2 mmol of $C_6H_{12}N_4$ were dissolved and stirred for 30 minutes. After this the solution has been transferred to the 100 mL autoclave containing NF and kept in oven at 130°C for 10 h. After this the obtained NF-LDH was washed and dried in the over at 60°C for 12 h.

Fabrication of the CNF-LDH:

The fabrication process for the CNF-LDH is also like the NF-LDH except the addition of the 0.15 mmol of the $Ce(NO_3)_3.6H_2O$ in the same solution.

Fabrication of the CNF-LDH-E:

After the synthesis of the CNF-LDH-E the electrode was immersed in the highly diluted acid solution of HCl (0.1 mM), the solution was heated in the sealed tube at 85°C for the 8 h. After this the electrode was removed, washed properly with ethanol and water and dried. The obtained electrode was further subjected to the nonthermal oxygen plasma treatment for the 120 seconds. Finally, the electrode was dipped in the 0.5 M $NaBH_4$ solution for the 30 min. The as obtained CNF-LDH-E was cleaned and dried properly for the further use. Similar method was used for the fabrication of the NF-LDH-E.

X-ray absorption spectroscopy

The synchrotron-based X-ray absorption spectroscopy was performed on 1D, 8C, and 10D beamlines of the Pohang Acceleration Laboratory (PAL, Korea) in top-up mode at 3.0 GeV with maximum ring current of 300 mA. To ensure accurate measurements, the harmonics of the incident X-ray beam were adjusted using a double crystal monochromator (DCM) with Si(111) crystals. Prior to data acquisition, energy calibration was performed using reference metallic foils. Specifically, Ir, Ni and Re transmission mode was employed to acquire the XAS data, with Fe, Ni and Ce metallic foils serving as reference standards. Subsequent data analysis was conducted using the ATHENA software suite[1, 2]. For the visualization of wavevector and interatomic distance (R) data in three dimensions, continuous Cauchy Wavelet Transform (CCWT) analysis was conducted. The analysis utilized k^2-weighted signals over a k-space range of 2.0 – 12.0 $Å^{-1}$. Near Edge X-ray Absorption Fine Structure (NEXAFS) spectra were obtained for the Ni K, Fe K and Ce L_3 edges, at the 10D beamline equipped with a bending magnet at PAL. Measurements were performed at room temperature with a resolution of 0.01 eV. Spectra were acquired in both total electron yield (TEY) and fluorescence yield (FY) modes under a base pressure of 3×10^{-10} Torr.

Electrochemical measurements

The electrocatalytic performance was assessed using a three-electrode system connected and operated by a potentiostation (Autolab PGSTAT; Metrohm) under alkaline and seawater conditions (1M KOH, 1M KOH+ 0.5 M NaCl). The three-electrode system contains the self-standing catalysts as a working electrode, Ag/AgCl is used as a reference electrode and graphitic electrode as a counter electrode. Purging of the N_2 in the electrolyte was performed before starting any electrochemical measurement. The exposed surface area of the working electron in the electrolyte was 1 Cm^2. The ink preparation for the IrO_2 and Pt/C was carried out by using 5 mg of each sample and dissolved in the 490 µL of the ethanol and 10 µL of nafion. Out of this 30 µL was drop casted over the nickel foam (NF). All the polarization curves were taken at the scan rate of the 5mV s^{-1}. The conversion of the potential to the reversible hydrogen electrode (RHE) by performed by the equation, E(RHE) = E(Ag/AgCl) + 0.059 pH + E^o (Ag/AgCl). 90% iR correction were performed to the polarization curves. Electrochemical impedance spectroscopy (EIS) was performed at 1.57 V_{RHE} in a frequency range from 0.1 to 100 kHz with a sinusoidal amplitude of 5 mV. Tafel plots were obtained using the iR-corrected LSV polarization curves. The Tafel slopes were calculated using the equation: $\eta = b \log j + a$, where (b: Tafel slope, j: current density, η: overpotential).

Density functional theory calculations

The first-principle calculations were conducted based on density functional theory (DFT) using the exchange-correlation energy function correlated by Perdew-Burke-Ernzerhof (PBE) with the generalized gradient approximation (GGA). [1] Self-consistent electronic density functional and total energy was obtained with the pseudopotential using the Vienna *ab initio* simulation package (VASP) code [2]. The plane wave basis set extended to 520 eV energy cutoff. In cases of transition metal cations, the pseudopotentials involving electrons in *p* and *d* orbitals of Ni and Fe as valence electrons (*Ni_pv* and *Fe_pv*) were used. Also, GGA+U correction scheme for transition metal cations such as Ni and Fe was adopted to correct energy of strongly correlated *3d* orbitals. [3] The Hubbard U values on Ni and Fe used in this calculation were 6.2 eV and 5.3 eV, respectively. The self-consistent loop was repeated until the total energy difference of systems between the adjacent repeating steps were less than 10^{-5} eV. To calculate wave functions in the LDH, only *Γ*-point was considered in irreducible Brillouin zone. Two different slab models with the lowest surface energy of $Ni_{0.9}Fe_{0.1}(OH)_2$ (001) and Ni_3Fe (111) were generated to calculate surface reactions. Those slab models were optimized by conjugate-gradient method [4] with DFT-D2 Van der Waals energy correction [5] until the maximum Hellmann-Feynman force became in ±0.025 eV/Å.

Supplementary Notes

Supplementary Note 1. Calculation of electrochemical surface area (ECSA)

Cyclic voltammetry curves were taken in the non-faradaic range in N_2-saturated 1M KOH solution, Further the differences in the current densities (J_{anodic}-$J_{cathodic}$) were plotted against the multiple scan rates. The slope of this curve is the measured double-layer capacitance (C_{dl}).

The higher the C_{dl} higher will be the ECSA. The specific capacitance used for the calculation of the ECSA is 0.04 mF cm^{-2}. Then, the ECSA is calculated using the formula.

$$ECSA = \frac{C_{dl}\ of\ the\ catalyst\ (mF\ cm^{-2})}{0.04\ (mF\ cm^{-2})}$$

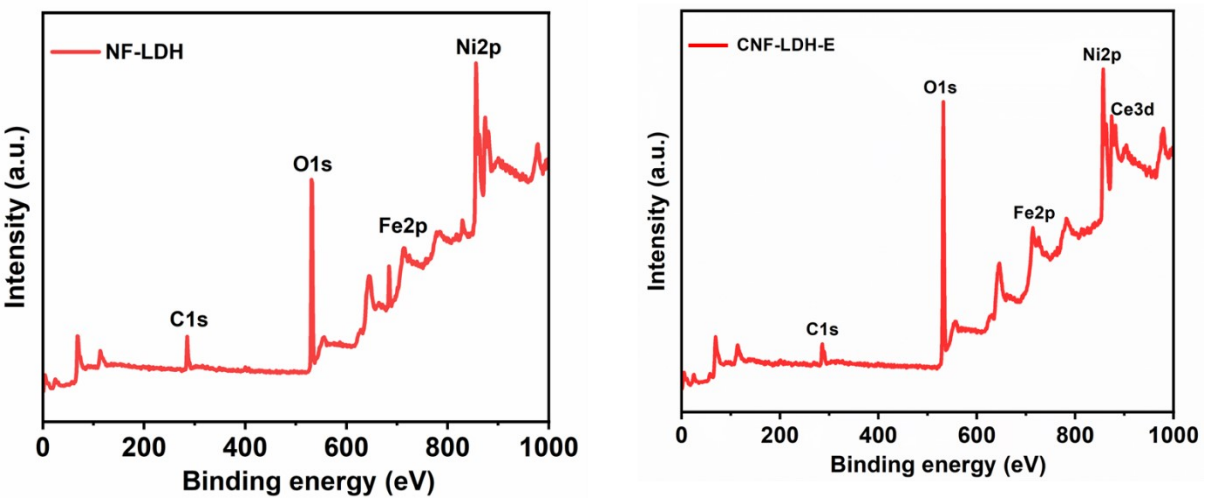

Figure S1. XPS survey spectra of the NF-LDH and CNF-LDH-E

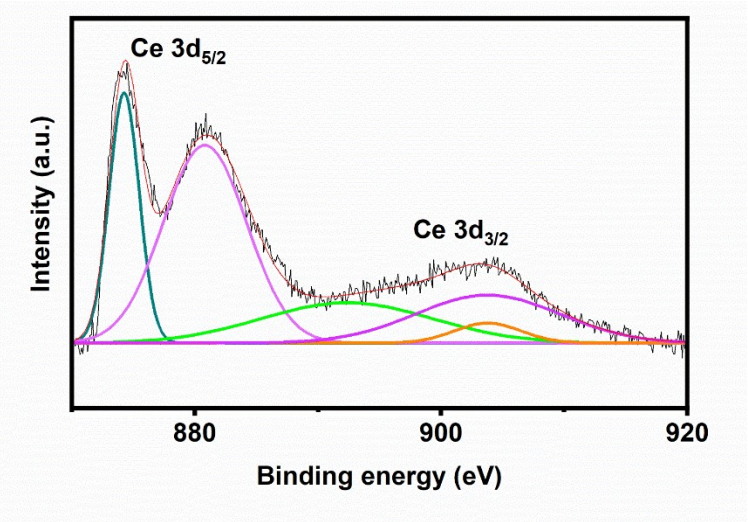

Figure S2: XPS spectra of the Ce3d present in CNF-LDH-E

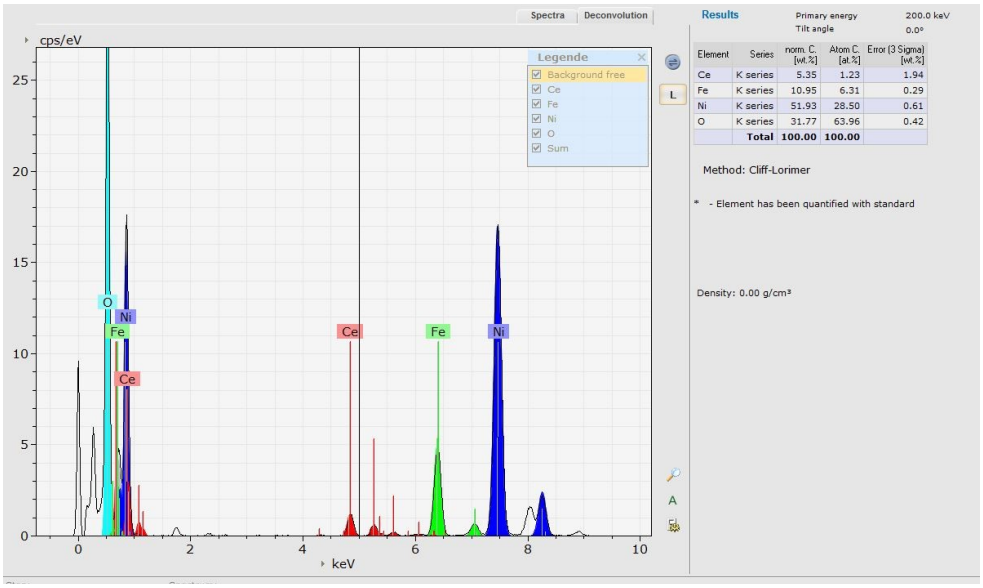

Figure S3. Atomic percentage of the Ce, Ni, Fe and O present in the catalyst by EDX

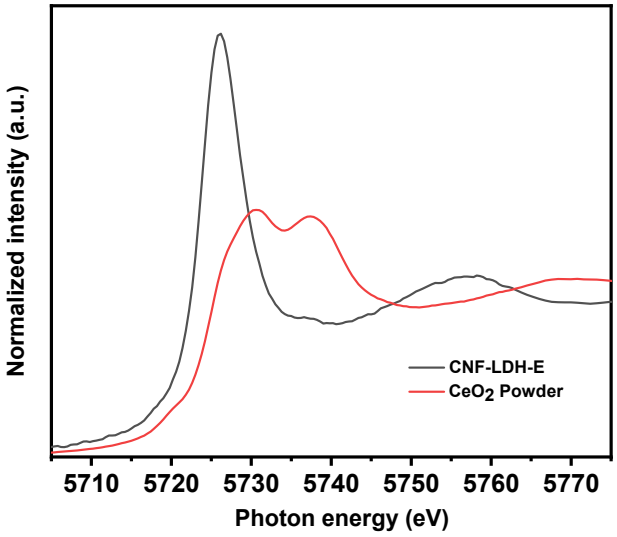

Figure S4. XANES spectra of Ce-L3 edge

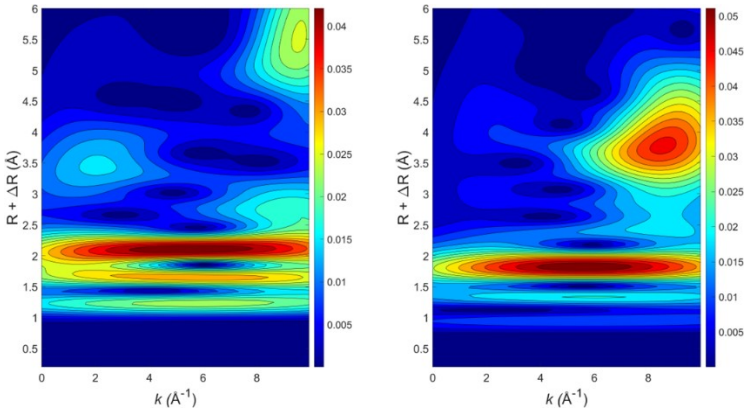

Figure S5: CCWT plot of Ce-L3edge in CNF-LDH-E and CeO_2

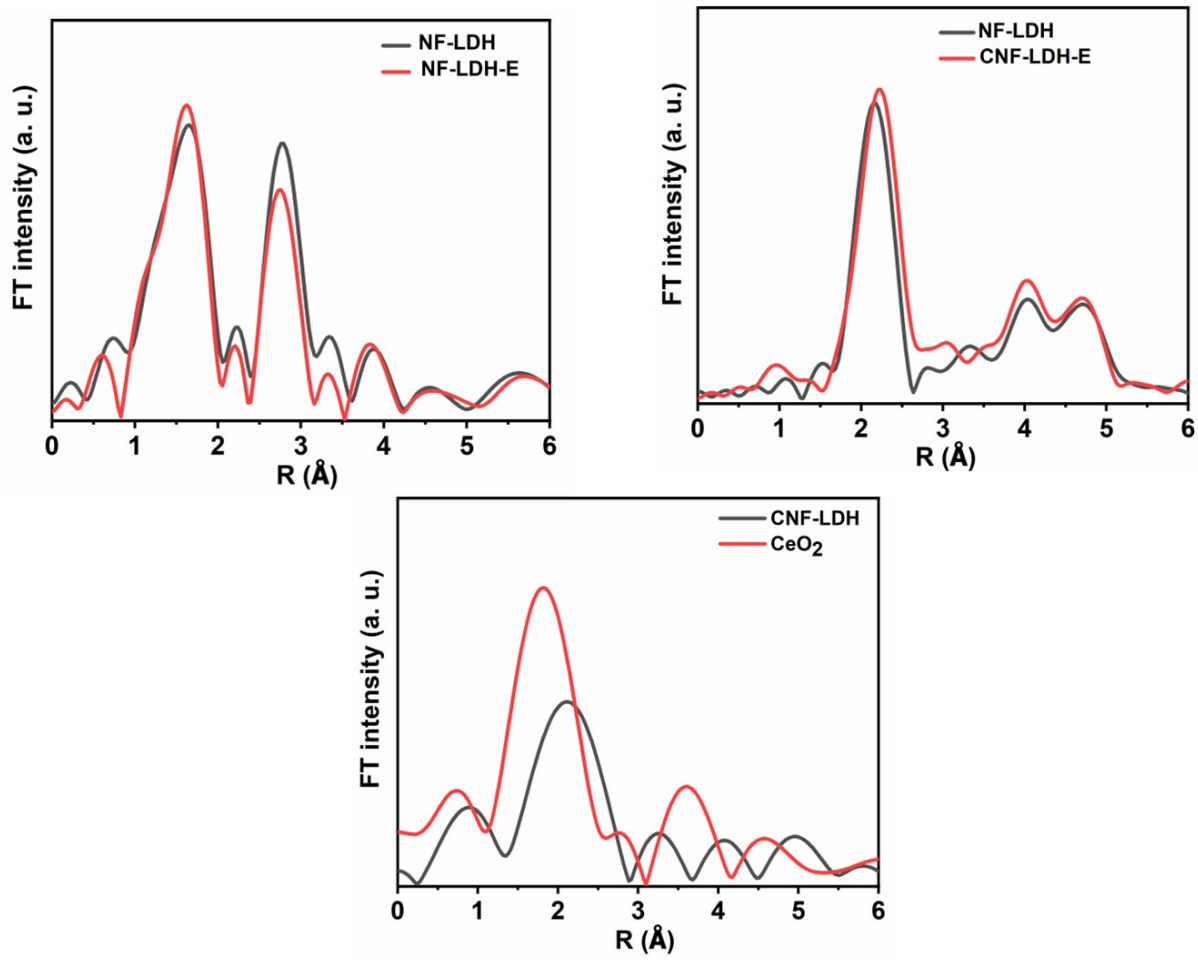

Figure S6: EXAFS spectra of Fe-Ledge, Ni-Kedge and Ce-L3edge

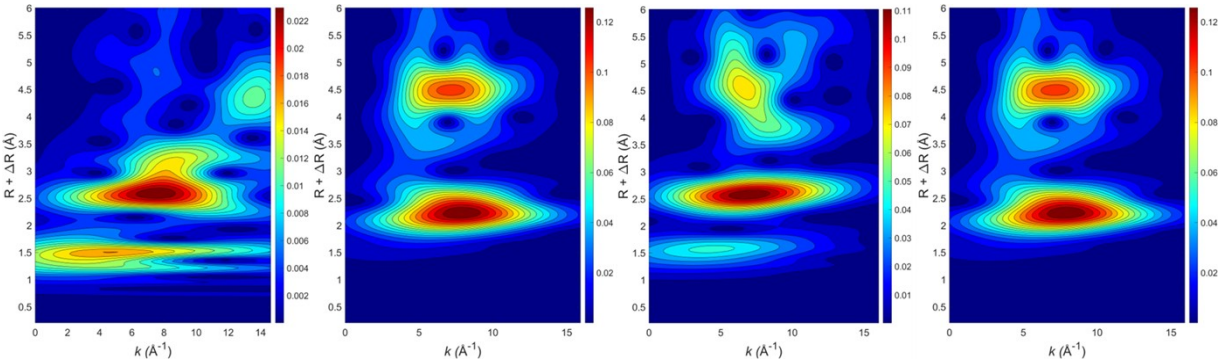

Figure S7: CCWT plot of Fe2O3, Fe-foil, NiO and Ni-foil

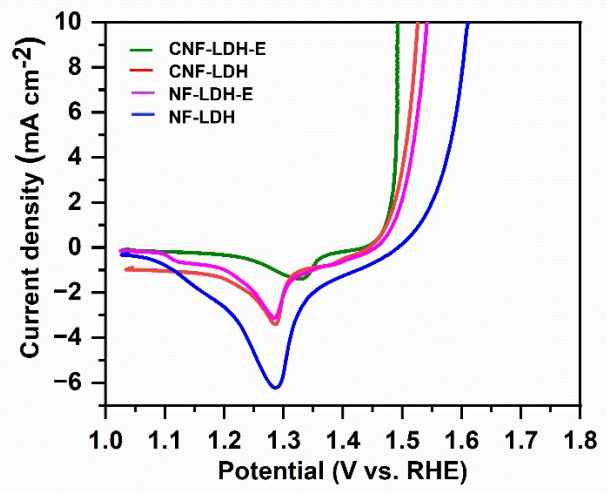

Figure S8: ECSA normalized OER activity

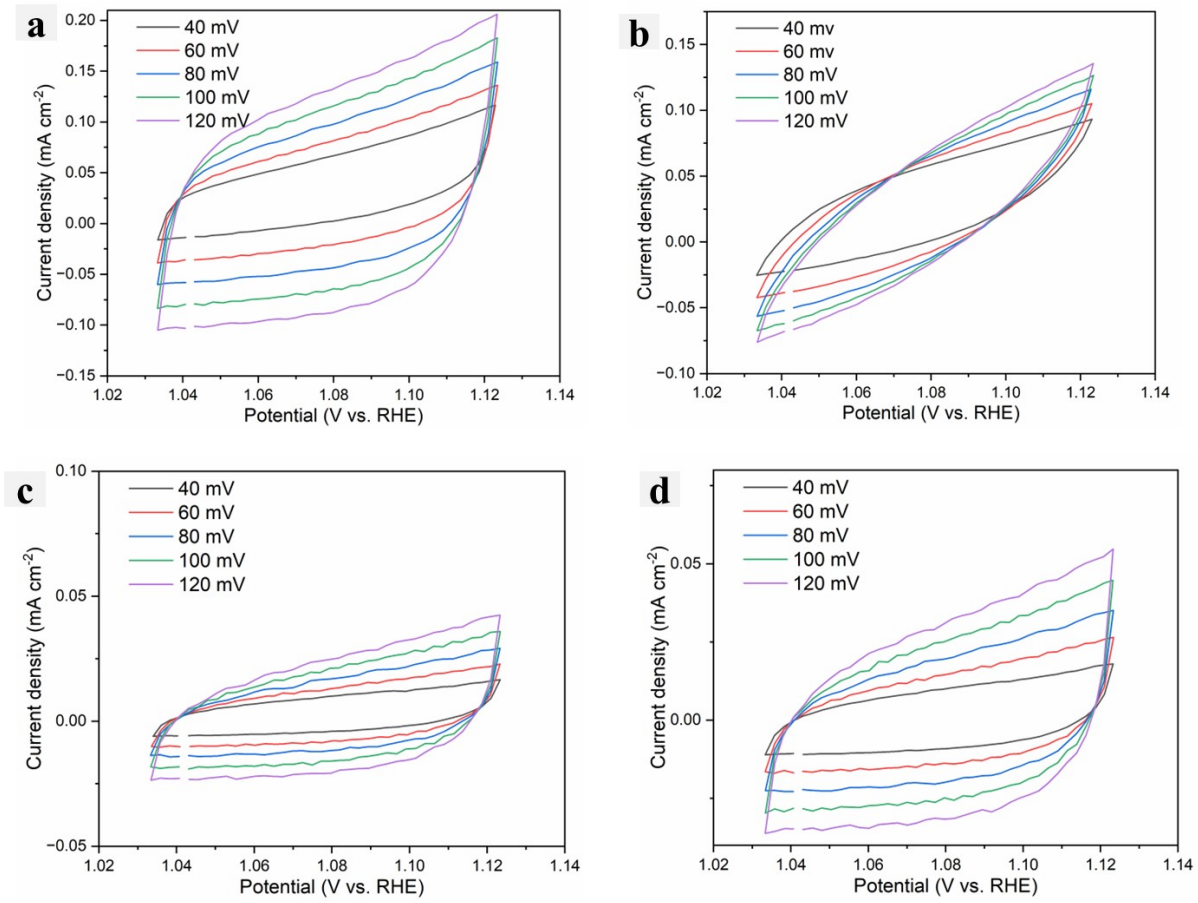

Figure S9: cyclic voltammetry curve in the non-faradaic region for the (a) CNF-LDH-E, (b) CNF-LDH, (C) NF-LDH-E, (e) NF-LDH

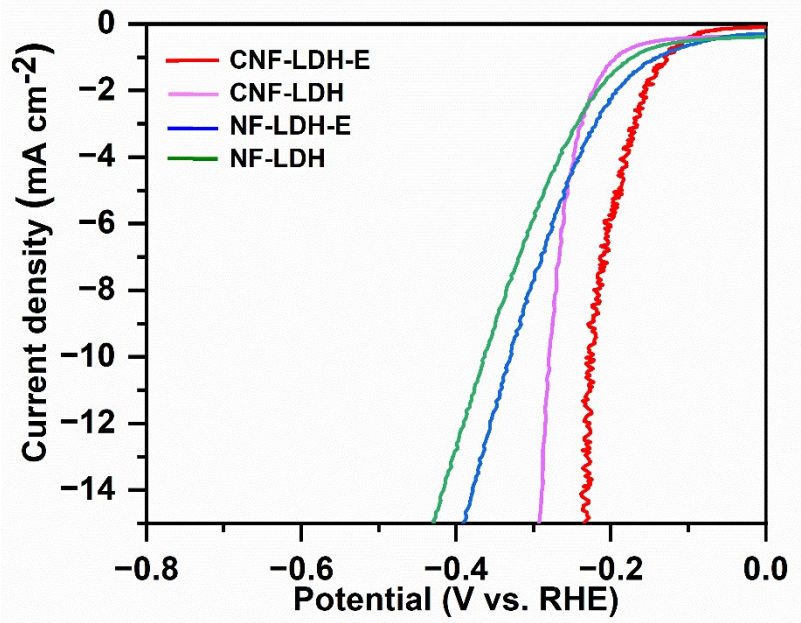

Figure S10: ECSA normalized LSV curve for the HER

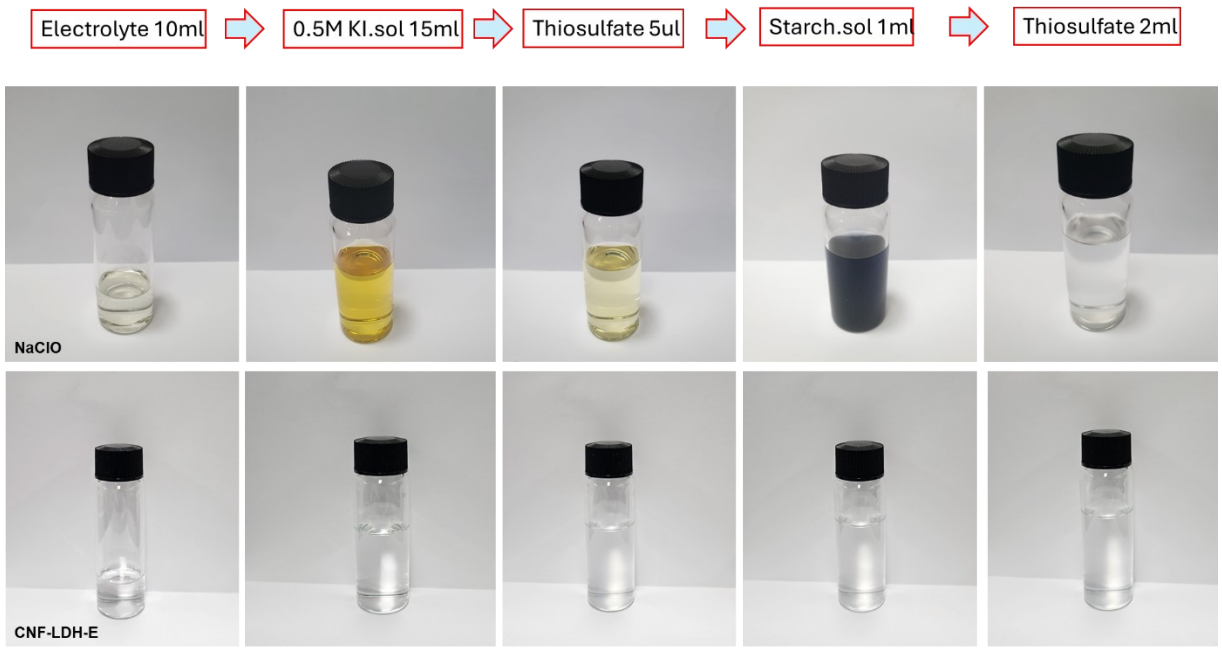

Figure S11: Digital photographs for iodide titration experiments for (upper) NaClO reference solution and (lower) the electrolyte solution after 30 h at 100 mA cm^{-2} in 1 M KOH and 0.5 M NaCl using CNF-LDH-E as a working electrode.

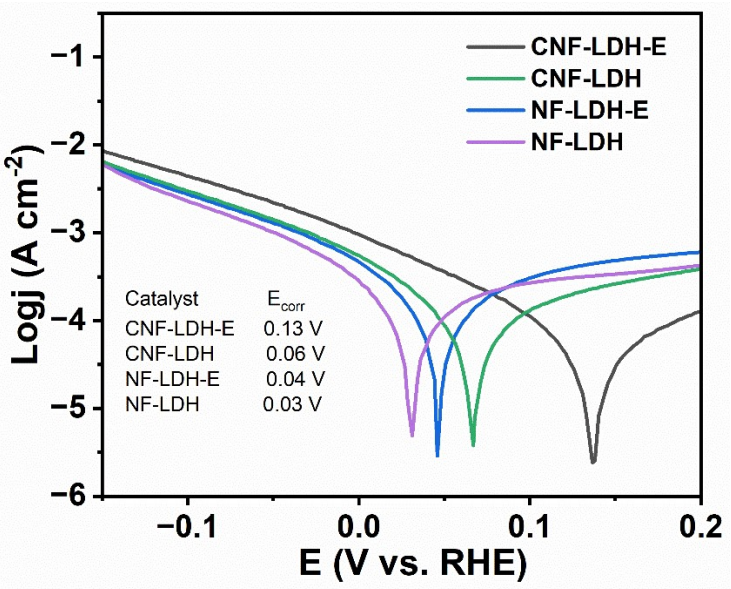

Figure S12. Tafel plots of all the catalyst in the electrolyte containing 1M KOH + 0.5 M NaCl

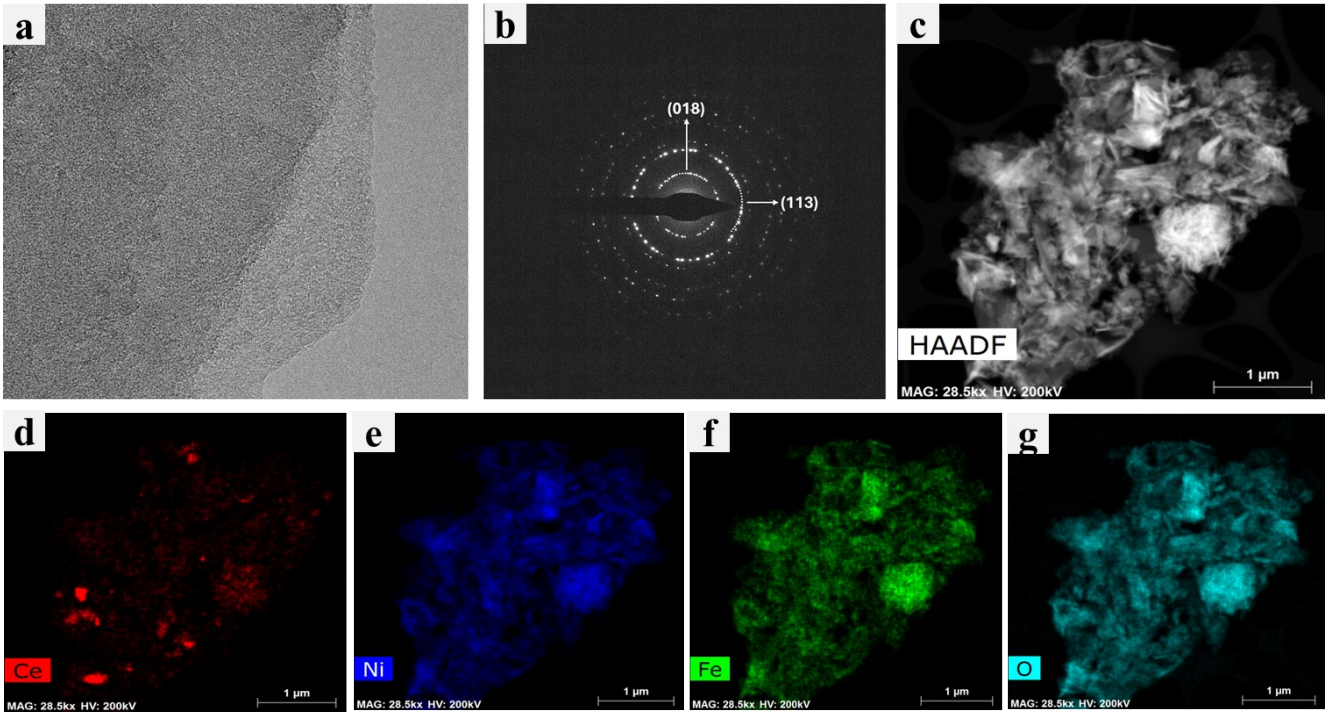

Figure S13: (a) TEM image of the catalyst after durability test for HER, (b) SAED pattern, (c-g) STEM-EDS mapping

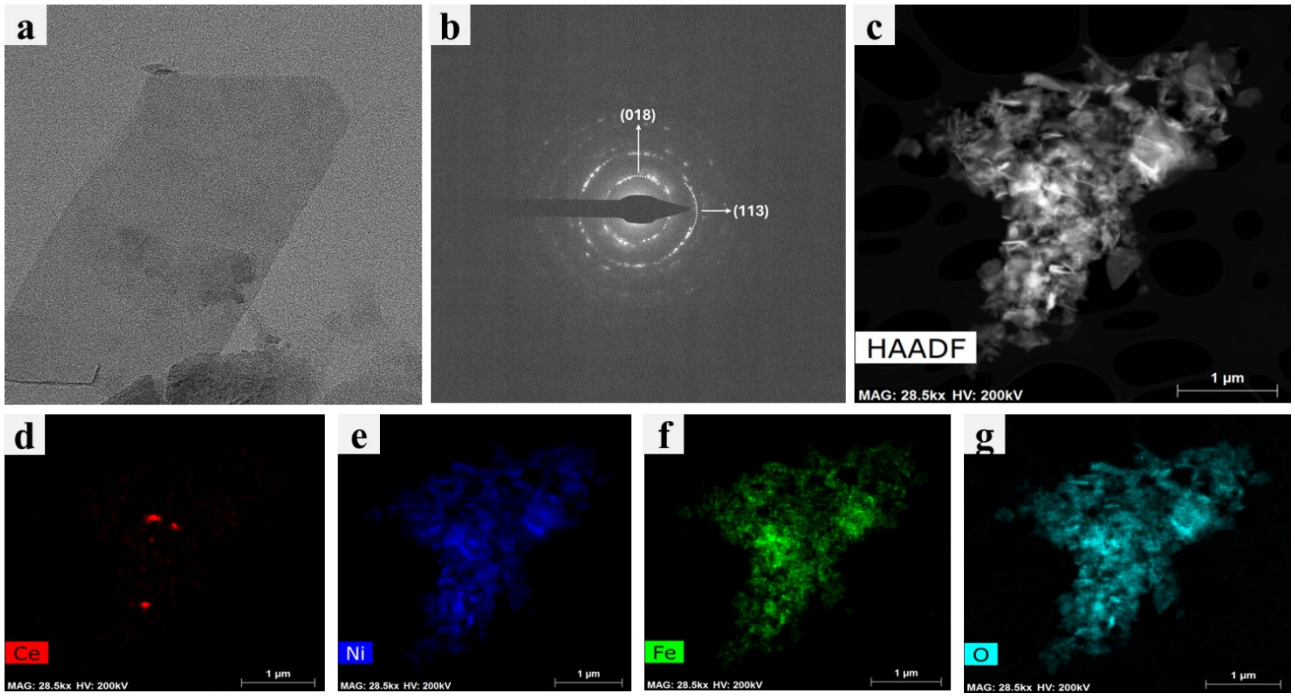

Figure S14: (a) TEM image of the catalyst after durability test for OER, (b) SAED pattern, (c-g) STEM-EDS mapping

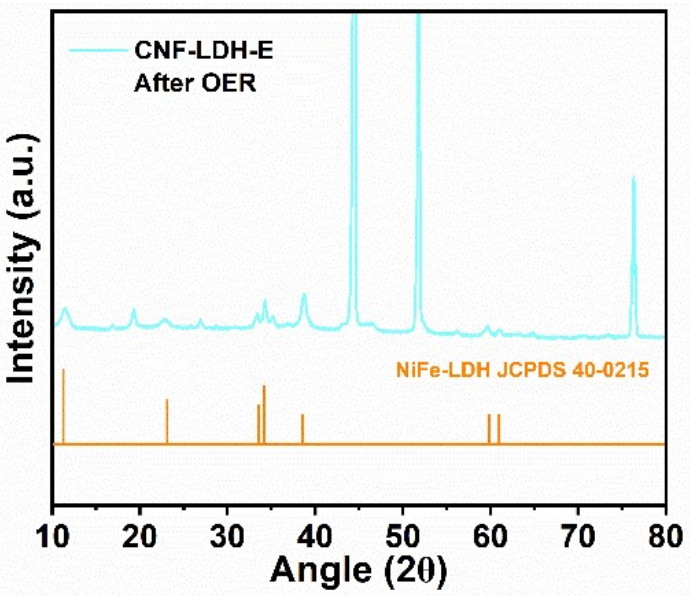

Figure S15: PXRD pattern of the catalyst after durability test for OER

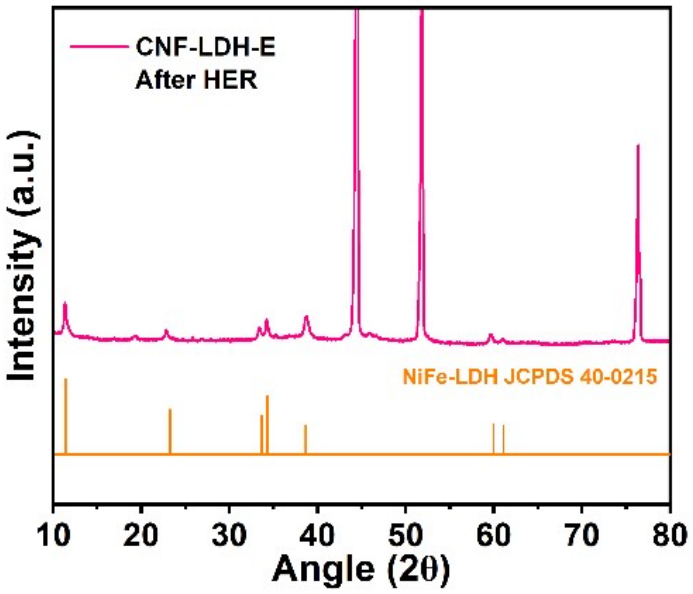

Figure S16: PXRD pattern of the catalyst after durability test for OER

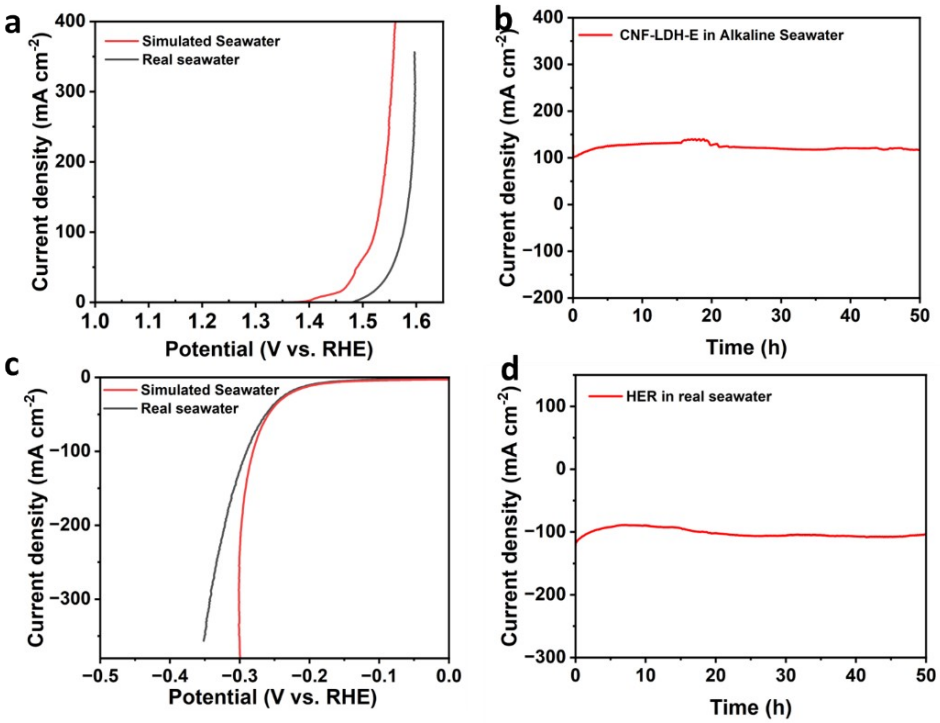

Figure S17. (a) polarization curve of the catalyst in the real alkaline seawater for OER (b) corresponding durability test (c) Polarization curve of CNF-LDH-E for the HER (d) corresponding durability test.

Table S1: Comparison of the overall water splitting behavior of our catalyst with the recently publishes state of the art catalyst in 1M KOH

Catalyst	Overpotential (HER) (mV)	Overpotential (OER) (mV)	Reference (Journal)
Ir@Ni-NDC	74@10 $mAcm^{-2}$	210@10 $mAcm^{-2}$	6 (Angew. Chem.)
CPF-Fe/Ni	201@10 $mAcm^{-2}$	194@10 $mAcm^{-2}$	7 (Nature Comm.)
Ni_2P/FeP-FF	42@10 $mAcm^{-2}$	217@10 $mAcm^{-2}$	8 (AFM)
Ru@V-RuO_2	201@10 $mAcm^{-2}$	6@10 $mAcm^{-2}$	9 (Adv. Mater.)
V-NiS/NiS_2	94@10 $mAcm^{-2}$	220@10 $mAcm^{-2}$	10 (Adv. Energy Mater.)
Mn-NiCoP	148@100 $mAcm^{-2}$	266@100 $mAcm^{-2}$	11 (Nano Energy)
Ni_2P-MnP@Co_2P	60@10 $mAcm^{-2}$	255@30 $mAcm^{-2}$	12 (Appl. Cat. B)
$FeNi(OH)_x$@NF	210@50 $mAcm^{-2}$	198@10 $mAcm^{-2}$	13 (Small)
CuNi@NiSe	42@10 $mAcm^{-2}$	293@10 $mAcm^{-2}$	14 (Small)
Mo-NIFeP/NIF	186@50 $mAcm^{-2}$	227@50 $mAcm^{-2}$	15 (Chem. Eng. J.)
$MnCo_2S_4$@MoS_2	208@1000 $mAcm^{-2}$	332@1000 $mAcm^{-2}$	16 (Chem. Eng. J.)
$AF_{0.1}$-FNMO/IF	345@500 $mAcm^{-2}$	289@500 $mAcm^{-2}$	17 (CCL)
Fe_2P/Co_2N	131@500 $mAcm^{-2}$	283@500 $mAcm^{-2}$	18 (AFM)
IF-Ni 150 mM	128@100 $mAcm^{-2}$	-	19 (ACS Nano)
CNF-LDH-E	**162@100 $mAcm^{-2}$**	**154@100 $mAcm^{-2}$**	**This work**

Table S2: Comparison of the overall water splitting behavior of our catalyst with the recently publishes state of the art catalyst in 1M KOH+0.5M NaCl

Catalyst	Overpotential (HER) (mV)	Overpotential (OER) (mV)	Reference (Journal)
$Fe_{0.74}Co_{0.26}$)2P/Ni3N	113@100 $mAcm^{-2}$	212@100 $mAcm^{-2}$	20 (Small)
RuNCs/P,O-NiFeLDH/NF	175@10 $mAcm^{-2}$	29@10 $mAcm^{-2}$	21 (AFM)
Ni_2P-Fe_2P	252@100 $mAcm^{-2}$	305@100 $mAcm^{-2}$	22 (AFM)
c-NF//a-NF-LDH NS	200@100 $mAcm^{-2}$	300@100 $mAcm^{-2}$	23 (AFM)
NiMoN@NiFeN	--	286@100 $mAcm^{-2}$	24 (Nature Comm.)
Mn-doped Ni_2P/Fe_2P	470@1000 $mAcm^{-2}$	358@1000 $mAcm^{-2}$	25 (Chem. Eng. J.)
N-$NiMo_3P$	35@10 $mAcm^{-2}$	346@10 $mAcm^{-2}$	26 (Small)
FMCO/NF	248@50 $mAcm^{-2}$	328@50 $mAcm^{-2}$	27 (Appl. Cat. B)
Co_xP_v@NC	206@500 $mAcm^{-2}$	323@500 $mAcm^{-2}$	28 (Nano energy)
NiFeLDH/FeOOH	181@10 $mAcm^{-2}$	286@100 $mAcm^{-2}$	29 (ACS IC)
CNF-LDH-E	**281@100 $mAcm^{-2}$**	**290@100 $mAcm^{-2}$**	**This work**

Table S3. Surface energies pf the different plane obtained from the DFT calculations

Plane	Total E (eV)		surface area X 2	surface E (eV/A3)
(001)_surf	-213.082	$Ce_1Fe_2Ni_5O_{16}H_{16}$	151.602816	0.012
(010)_surf	-209.268	$Ce_1Fe_2Ni_5O_{16}H_{16}$	60.092672	0.093
(100)_surf	-211.263	$Ce_1Fe_2Ni_5O_{16}H_{16}$	104.824884	0.034
(110)_surf	-209.61	$Ce_1Fe_2Ni_5O_{16}H_{16}$	120.823464	0.044
(111)_surf	-415.042	$Ce_2Fe_4Ni_{10}O_{32}H_{32}$	285.539084	0.051
(012)_surf	-1070.069	$Ce_5Fe_{10}Ni_{25}O_{80}H_{80}$	306.5281044	0.014

References for SI

1. Perdew, J. P.; Burke, K.; Ernzerhof, M. Generalized Gradient Approximation Made Simple. *Phys. Rev. Lett.* 77, 18, 3865 (1996).
2. Kresse, G.; Furthmüller, J. Efficient iterative schemes for ab initio total-energy calculations using a plane-wave basis set. *Phys. Rev. B* 54, 16, 11169 (1996).
3. Wang, L.; Maxisch, T.; Ceder, G. Oxidation energies of transition metal oxides within the GGA+ U framework. *Phys. Rev. B* 73, 195107 (2006).
4. Hestenes, M. R.; Steifel, E.; Methods of Conjugate Gradients for Solving. J. Res. Natl. Bur. Stand. 49, 409 (1952).
5. Grimme, S. Semiempirical GGA-type density functional constructed with a long-range dispersion correction. *J. Comput., Chem.* 27, 1787 (2006).
6. Yang, J., Shen, Y., Sun, Y., Xian, J., Long, Y. and Li, G., 2023. Ir nanoparticles anchored on metal-organic frameworks for efficient overall water splitting under pH-universal conditions. *Angewandte Chemie*, *135*(17), p.e202302220.
7. Zang, Y., Lu, D.Q., Wang, K., Li, B., Peng, P., Lan, Y.Q. and Zang, S.Q., 2023. A pyrolysis-free Ni/Fe bimetallic electrocatalyst for overall water splitting. *Nature Communications*, *14*(1), p.1792.
8. Jiang, M., Zhai, H., Chen, L., Mei, L., Tan, P., Yang, K. and Pan, J., 2023. Unraveling the synergistic mechanism of Bi-functional nickel–iron phosphides catalysts for overall water splitting. *Advanced Functional Materials*, *33*(33), p.2302621.
9. Li, Y., Wang, W., Cheng, M., Feng, Y., Han, X., Qian, Q., Zhu, Y. and Zhang, G., 2023. Arming Ru with oxygen-vacancy-enriched RuO2 sub-nanometer skin activates superior bifunctionality for pH-universal overall water splitting. *Advanced Materials*, *35*(24), p.2206351.
10. Xu, W., Zhao, R., Li, Q., Sun, B., Wu, J., Zhong, W., Gao, Y., Nan, X., Huang, Q., Yang, Y. and Li, X., 2023. Overall Water Splitting on The NiS/NiS2 Heterostructures Featuring Self-Equilibrium Orbital Occupancy. *Advanced Energy Materials*, *13*(31), p.2300978.
11. Ma, G., Ye, J., Qin, M., Sun, T., Tan, W., Fan, Z., Huang, L. and Xin, X., 2023. Mn-doped NiCoP nanopin arrays as high-performance bifunctional electrocatalysts for sustainable hydrogen production via overall water splitting. *Nano Energy*, *115*, p.108679.
12. Kandel, M.R., Pan, U.N., Dhakal, P.P., Ghising, R.B., Nguyen, T.T., Zhao, J., Kim, N.H. and Lee, J.H., 2023. Unique heterointerface engineering of Ni2P− MnP nanosheets coupled Co2P nanoflowers as hierarchical dual-functional electrocatalyst for highly proficient overall water-splitting. *Applied Catalysis B: Environmental*, *331*, p.122680.
13. Li, B., Zhao, J., Wu, Y., Zhang, G., Wu, H., Lyu, F., He, J., Fan, J., Lu, J. and Li, Y.Y., 2023. Identifying Fe as OER active sites and ultralow-cost bifunctional electrocatalysts for overall water splitting. *Small*, *19*(37), p.2301715.
14. Cao, D., Shao, J., Cui, Y., Zhang, L. and Cheng, D., 2023. Interfacial engineering of copper–nickel selenide nanodendrites for enhanced overall water splitting in alkali condition. *Small*, *19*(33), p.2301613.
15. Wang, Y., Yang, P., Gong, Y., Liu, D., Liu, S., Xiao, W., Xiao, Z., Li, Z., Wu, Z. and Wang, L., 2023. Amorphous high-valence Mo-doped NiFeP nanospheres as efficient electrocatalysts for

overall water-splitting under large-current density. *Chemical Engineering Journal*, *468*, p.143833.
16. Ma, T., Shen, X., Jiao, Q., Zhao, Y., Li, H., Zhang, Y., Lv, Y., Feng, C. and Guo, L., 2023. In-situ construction of hexagonal-star-shaped MnCo2S4@ MoS2 boosting overall water splitting performance at large-current-density: Compositional-electronic regulation, functions, and mechanisms. *Chemical Engineering Journal*, *464*, p.142592.
17. Zhang, X.Y., Yu, W.L., Zhao, J., Fu, J.Y., Dong, B., Wang, F.L., Yu, J.F., Liu, C.G. and Chai, Y.M., 2023. Self-supported FexNi1-xMoO4 with synergistic morphology and composition for efficient overall water splitting at large current density. *Chinese Chemical Letters*, *34*(2), p.107422.
18. Zhou, X., Mo, Y., Yu, F., Liao, L., Yong, X., Zhang, F., Li, D., Zhou, Q., Sheng, T. and Zhou, H., 2023. Engineering active iron sites on nanoporous bimetal phosphide/nitride heterostructure array enabling robust overall water splitting. *Advanced Functional Materials*, *33*(6), p.2209465.
19. Yu, D., Hao, Y., Han, S., Zhao, S., Zhou, Q., Kuo, C.H., Hu, F., Li, L., Chen, H.Y., Ren, J. and Peng, S., 2023. Ultrafast combustion synthesis of robust and efficient electrocatalysts for high-current-density water oxidation. *ACS nano*, *17*(2), pp.1701-1712.
20. Ma, W., Li, D., Liao, L., Zhou, H., Zhang, F., Zhou, X., Mo, Y. and Yu, F., 2023. High-Performance Bifunctional Porous Iron-Rich Phosphide/Nickel Nitride Heterostructures for Alkaline Seawater Splitting. *Small*, *19*(19), p.2207082.
21. Chen, W., Wei, W., Li, F., Wang, Y., Liu, M., Dong, S., Cui, J., Zhang, Y., Wang, R., Ostrikov, K. and Zang, S.Q., 2024. Tunable Built-In Electric Field in Ru Nanoclusters-Based Electrocatalyst Boosts Water Splitting and Simulated Seawater Electrolysis. *Advanced Functional Materials*, *34*(7), p.2310690.
22. Wu, L., Yu, L., Zhang, F., McElhenny, B., Luo, D., Karim, A., Chen, S. and Ren, Z., 2021. Heterogeneous bimetallic phosphide Ni2P-Fe2P as an efficient bifunctional catalyst for water/seawater splitting. *Advanced Functional Materials*, *31*(1), p.2006484.
23. Enkhtuvshin, E., Yeo, S., Choi, H., Kim, K.M., An, B.S., Biswas, S., Lee, Y., Nayak, A.K., Jang, J.U., Na, K.H. and Choi, W.Y., 2023. Surface reconstruction of Ni–Fe layered double hydroxide inducing chloride ion blocking materials for outstanding overall seawater splitting. *Advanced Functional Materials*, *33*(22), p.2214069.
24. Yu, L., Zhu, Q., Song, S., McElhenny, B., Wang, D., Wu, C., Qin, Z., Bao, J., Yu, Y., Chen, S. and Ren, Z., 2019. Non-noble metal-nitride based electrocatalysts for high-performance alkaline seawater electrolysis. *Nature communications*, *10*(1), p.5106.
25. Luo, Y., Wang, P., Zhang, G., Wu, S., Chen, Z., Ranganathan, H., Sun, S. and Shi, Z., 2023. Mn-doped nickel–iron phosphide heterointerface nanoflowers for efficient alkaline freshwater/seawater splitting at high current densities. *Chemical Engineering Journal*, *454*, p.140061.
26. Loomba, S., Khan, M.W., Haris, M., Mousavi, S.M., Zavabeti, A., Xu, K., Tadich, A., Thomsen, L., McConville, C.F., Li, Y. and Walia, S., 2023. Nitrogen-doped porous nickel molybdenum phosphide sheets for efficient seawater splitting. *Small*, *19*(18), p.2207310.
27. Liu, W., Que, W., Yin, R., Dai, J., Zheng, D., Feng, J., Xu, X., Wu, F., Shi, W., Liu, X. and Cao, X., 2023. Ferrum-molybdenum dual incorporated cobalt oxides as efficient bifunctional anti-corrosion electrocatalyst for seawater splitting. *Applied Catalysis B: Environmental*, *328*, p.122488.
28. Wang, X., Liu, X., Wu, S., Liu, K., Meng, X., Li, B., Lai, J., Wang, L. and Feng, S., 2023.

Phosphorus vacancies enriched cobalt phosphide embedded in nitrogen doped carbon matrix enabling seawater splitting at ampere-level current density. *Nano Energy*, *109*, p.108292.
29. Jiang, K., Liu, W., Lai, W., Wang, M., Li, Q., Wang, Z., Yuan, J., Deng, Y., Bao, J. and Ji, H., 2021. NiFe layered double hydroxide/FeOOH heterostructure nanosheets as an efficient and durable bifunctional electrocatalyst for overall seawater splitting. *Inorganic chemistry*, *60*(22), pp.17371-17378.